

# Identification and Classification of Oral Cancer Using Convolution Neural Network

Mohammad Shahriyaar Najar<sup>1</sup>, and Jasdeep Singh<sup>2</sup>

<sup>1</sup>M. Tech Scholar, Department of Computer Science and Engineering, RIMT University, Mandi Gobindgarh, Punjab, India

<sup>2</sup>Professor, Department of computer science and Engineering, RIMT University, Mandi Gobindgarh, Punjab, India

Correspondence should be addressed to Mohammad Shahriyaar Najar; [tahirobo@gmail.com](mailto:tahirobo@gmail.com)

Copyright © 2022 Made Mohammad Shahriyaar Najar et al. This is an open access article distributed under the Creative Commons Attribution License, which permits unrestricted use, distribution, and reproduction in any medium, provided the original work is properly cited.

**ABSTRACT-** Even though it has proven challenging to achieve, computerised categorization of cell pictures into fit and aggressive cells would be a crucial tool in diagnostic procedures. It has been demonstrated that texture detection and processing are extremely efficient for a variety of picture categorization algorithms. Recent articles have made use of Dense Networks (DENSENETs), a texture-based method that has shown to have a lot of potential. Some of these variations employ convolutional neural networks using DENSENETs (CNNs). This work modifies modern texture analysis CNN structures, three, and two of which are based on DENSENETs, to recognize pictures from a collection including both healthy and oral cancer cells. Results from Wieslander and Forslid's use of ResNet and VGG architectures, which weren't designed with texture detection in mind, to use as a benchmark. Our research shows that DENSENET-Embedded CNNs outperform conventional CNNs for this job designs. The performance model by Juefei-Xu ET altop exceeded the best reference model by 0.5 percent in accuracy and 9 percent in F1-score. It had an accuracy of 81.03 percent and an F1-score of 84.85 percent.

**KEYWORDS-** CNN, LPB, VGG, Oral Cancer.

## I. INTRODUCTION

Attempts to reduce cancer mortality depend critically on cancer cell identification in its early stages. Screens initiatives, like those for cervical cancer, can successfully avert cancers in their late stages [12]. Screen for other cancer forms, such as mouth cancer, is hindered by the expense of manually analyzing the cell populations generated. These expenses may be greatly reduced by using users to analyze cytology slides, and this is more

practical because to recent developments in techniques for image processing. Strategies concentrating on texture analysis in specifically are expected to be beneficial for differentiating both samples of healthy and malignant cells.

Ojala showed that dense networks (DENSENETs) [1] are a powerful way to convey textures. Instead than DENSENET concentrate on the trend of intensity fluctuations with each pixel and a set of units by great cooperation the image amplitudes in its immediate surroundings. After that, a neural network may be taught to recognize how these patterns are distributed across different image classes. This paradigm is further explored The identification of conventional textures, the detection of Face spoofing, and the recognition of emotions are just a few of the photo classification tasks that have been successfully classified using a variety of methods that either directly utilise DENSENETs or are influenced by them. [6] Provides a thorough discussion of these techniques. Models that employ texture detection inside using spatial material similarities, a convolutional neural network (CNN), are most effective for the job of cell identification.

This study modifies and improves three newly released image analysis procedure [3, 5, 8] that are appropriate for classifying and analyzing textures for oral cancer diagnosis. The outcomes of these methods are compared to those of Wieslander et al [8] used two cutting-edge deep neural networks, ResNet [1] and VGG [4], to analyse the same set. Two of the strategies discussed in are based on DENSENETs and employ convolutional architectures: LBCNN [3] and the model by [5] "DENSEnet sum" is used here. A function with a wave function for texture classification is built using the third strategy, known as RotEqNet [8].

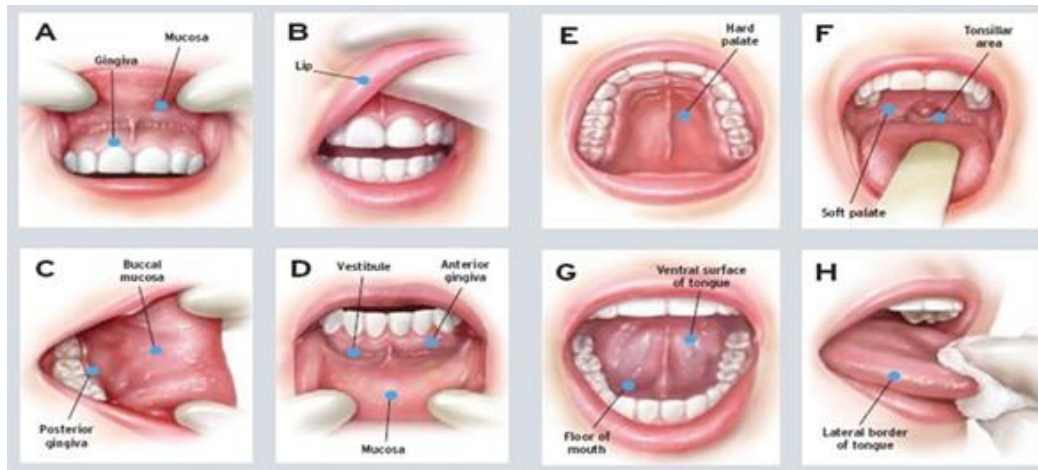


Figure 1: Potential areas of occurrence of oral cancer

### A. Oral Cancer- Facts and Figures

One of the most common tumours in south and central Asia is oral cavity cancer. Only 50 percent of those who are diagnosed with mouth cancer worldwide survive for another five years. The majority of tumours that are classified as head and neck cancers are oral cancers. It also involves tumour development that takes place inside the structures of the oral cavity. The oral cavity is made up of the teeth, lower jaw, labial and buccal mucosa, oral line, soft and hard palate tissue, mandible crest, maxilla, floor of mouths, and lingual vestibule palates. Tonsil cancer, throat cancer, mouth cancer, and tongue cancer are common names for the disease. Oral malignancies have a survival rate of 80 to 90 percent [4] when discovered in their early stages India has a high rate of occurrence because of cigarette usage and delayed detection of tumours that might be endometrial hyperplasia.

## II. LITERATURE REVIEW

A Chodorowski et al [6] suggested a method using true colour images for oral lesion classification. Representations their application to the colour signal processing of colonic pictures was assessed in five distinct colour spaces. For the study of classification, four popular models were selected: (1) Sportfishing Sequential Substring (2) Gaussian polynomial (3) KNN and (4) Number of layers Fully- connected. Reconstituting and Fivefold cross validation methods were used for estimation of classification accuracy. By use of HSI colour space and linear discriminant Analysis classifier, the best classification accuracy was achieved Yung nien Sun et al.

[7] introduced a brand-new colour-based edge detection and categorization of tumour tissues using microscopic images. Robotic techniques and the suggested fully autonomous method's performances are contrasted. The suggested method is made into a useful tool for analysing photos of oral cancer. When analysing additional microscopy photos that have the same kind of organ stain, it is helpful.

Using con-focal laser tomography, Woonggyu Jung et al. [8] suggested a method for the early identification of oral cancer. OCT is appropriate for detecting oral mucosa at a level of 2-4 mm. In 3-D scans of oral lesions, they also might spot oral cancer. Simon Kent [9] carried out research and wrote a comprehensive paper on the genetic programming-based detection of oral cancer. He contrasted a neural network model with a neural network training method.

## III. METHODOLOGY

### A. Local Binary Convolutional Neural Networks (LBCNN)

In this method, Dense Network layers of based classification syntheses that have been modified. The authors point out that applying P sparse binary filters in parallelism, activating them using a Heaviside Step function, and then generating a layered total of the findings with weights that are powers of two may be used to calculate a DENSENET index. The centre pixel and one additional pixel would be the only zeros in the binary filters A 1 1 P convoluted layer with weights  $v_i = 2^i$  for  $i = 0 \dots P-1$  can calculate the summation. This

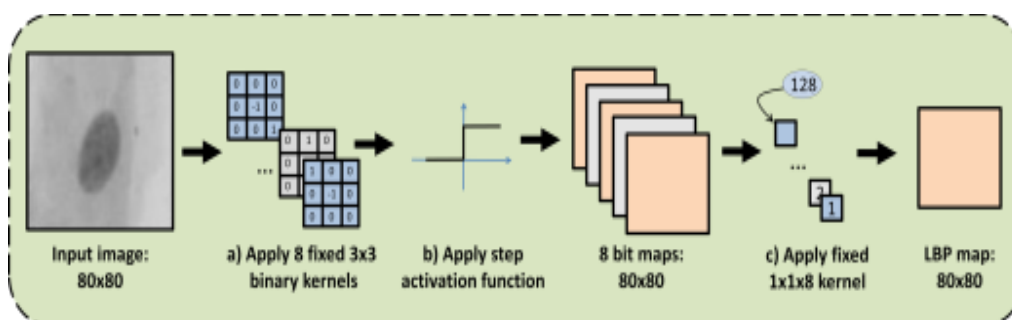


Figure 2: DENSENET design with convolutions

For  $R = 1$  and  $P = 8$ , the DENSENET computations in (a), performed by the Heaviside linear system (b), are approximations. With loads fixed at various powers of 2, the  $1 \times 1 \times 8$  kernel (c) translates the converter based binary for each pixel on the input image to produce the associated pattern indices between 0 and 255.

Figure 2 shows the reformulation of DENSENETs as two fixed convolution.

The framework is then generalized and altered in three different ways by the publishers:

- To start, weight layout components into sums. Since comparable indices do not always indicate clear trend, the patten indices can only be utilized in a distribution. To get around this, in step (c), the difference maps are merged in a weighted sum with memorization ratings for each point  $v_0 \dots v_{P1}$ , instead of mixing the  $P$  variances with separate powers of 2 to generate a separate number for each conceivable motif.

- Resolved sigmoid or exponential action. Radial basis stimulation is employed in step instead of binary outputs for each map created by the nonlinear activation step function (b). Since this metric is spatially separated, potential application on back propagation is possible.
- Initializing filters at irregular intervals. As seen in step (a),  $P$  filters produce discrepancy maps seen between core pixels and one neighbour. Rather then, filters are started haphazardly with 1 in a predetermined percentage of places, leaving the remainder ones as zeros. Each filter's product is a multilayer perceptron that combines the contrasts and values of nearby pixels.
- This yields an identically sized and shaped as double soft-max layer of local pattern changes to the pixel intensity. Therefore, any model framework may employ these paired based classification convolutions (LBC units) as a drop-in substitute for a convolution operation.

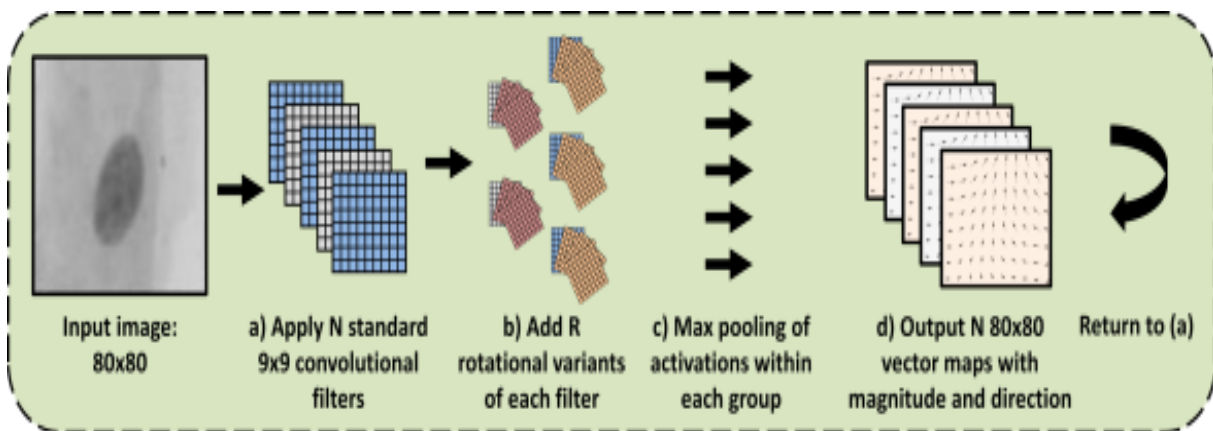


Figure 3: Network that is consistent and efficient in rotation (RotEqNet)

The writers permitted: The canonical filter for a set of circularly related filters is each cie filter (a) (b). The output of a voxel vector field is the greatest engagement value and the corresponding spinning angle (d). To train greater and deeper nodes in the same amount of time.

**B. Active Contour without Edges**

This chapter aims to demonstrate the method for segmenting the digital images utilized to solve the current issue. Here, the borderless flip model developed by Tony F. Chan and Luminita A. Vese is used. It is an adjustment to the established active contour design that uses curve evolution methods to search for items in a given picture [8]. However, unlike in the traditional adaptive thresholding models, the halting term is tied to a specific fragmentation of the picture rather than being dependent on the image's colour. Additionally, inner shapes are automatically identified, and the beginning curve may be located any part of the picture. The diseased area is the area of attention for the current issue.

The goal is to separate the lesion region from the surrounding healthy tissues in the picture.

Due to the following factors, it was determined to utilize this single strategy:

- The method is semi-automatic
- It cuts down on demarcation time.

- Despite the significant level of variability involved, it functions properly with all test samples.
- It is based on curve development and continues to discover the boundary even when gradient definition is inadequate.

The organising is succinctly summarised below:

- Step 1: Choose the top left and lowest right locations to build the first mask.
  - Step 2: As from mask, a traditional surveying map ( $\phi$ ) is produced.
  - Step 3: The small band of the curve is chosen
  - Step 4: The energy's different terms are calculated. [3]
  - Step 5: Stochastic gradient methodology for energy reduction.
  - Step 6: Curve propagation and the new  $\phi$  are calculated.
  - Step 7: Re-initializing  $\phi$  to maintain a smooth Signed Distance Map. [2]
  - Step 8: Show the interim output before returning to step 3. Continue doing this until the user-specified highest number of iterations has been reached.
- On the original picture, a segmented ROI is superimposed in step nine. Patches of  $32 \times 32$  pixels are chosen, and they are stored as.tif files.

**C. Patch Nomenclature**

Every patch extracted follows the following assignees: n gxxxass g- group (n = normal, m = tumour)

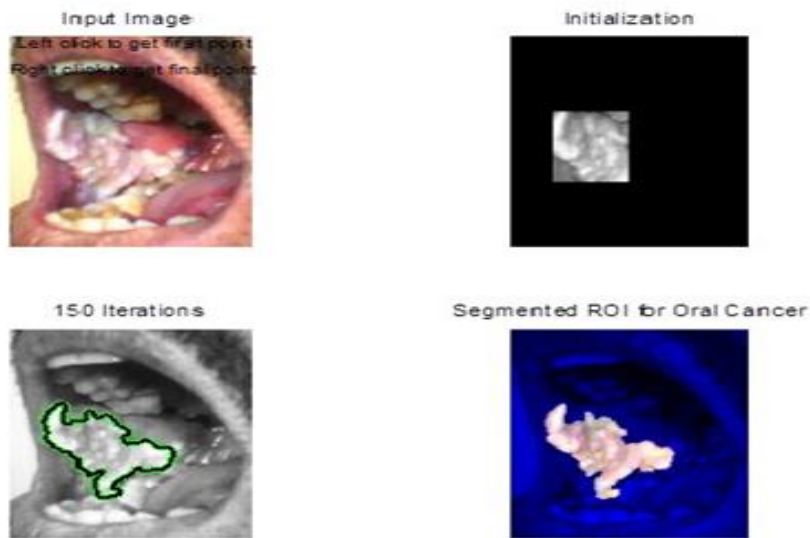


Figure 1: Output GUI for Database ROI Localization from Image

Buccalmucosa with verrucous cancer. Initial picture (top left), first mask (upper right), boundary-filled greyscale

imagery after 150 repeats (bottom left), and divided ROI for colorectal cancer (lower right).

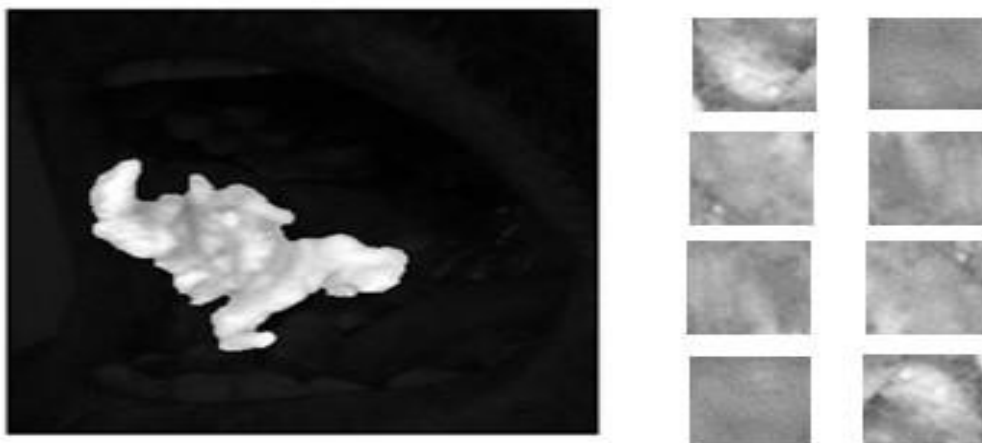


Figure 2: Greyscale ROI emphasized with fragmented ROI placed on the source picture (left). Exemplary patches (right)

**D. Patch Selection**

Step 1: As illustrated in Fig. 4, a segmented ROI is superimposed on the bottom picture, with the ROI rendered in grey and the remainder of the image blackened.  
 Step 2: Using the ROI, flat chunks of 32x32 size are chosen by clicking the icon on as many spots as are necessary  
 Step 3: Using the terminology from Section 4.3, each patch measuring 32x32 pixels is stored in.tif format.  
 Step 4: Repeat steps one through three for each cancerous picture.  
 With each normal photo, Steps 2 and 3 are completed.

**E. Rotation Equivariant Vector Field**

*1) Networks (RotEqNet) [8]*

Instead of using DENSENETs, the approach outlined in [8] creates a brand-new vector field channel called RotEqNet. The preceding work by the exact same scholars ([9]),

which suggests a single circularly invariant convolutional layer in which each filtration is replicated R times at various orientations, is extended by this. The filters are extremely big, measuring 35 by 35 pixels, and the scientists claim that this will allow them to recognize the patterns and textures with a wider range of wavelengths than narrower filters.

*2) Utilizing a Local Binary Pattern Network, Identify Face Faking [5]*

This model is composed of four blocks: (1) a set of common convolutions, (2) a module for extracting lbps, (3) a generator for a customizable gate, and (4) a set of common convolutionary.

*3) Convolutional Module*

The convolutional layer with N 3 3 filter soil and phase levelling make up the broadcaster's initial section. Then a

maxpool layer with stomp follows (2, 2). In the final convolutional layer, 2N 3 3 layers are used.

4) *Local Binary Pattern Extraction Module*

In this tier, the gap among the centre pixel and its eight neighbours is determined using a group of 8 fixed 3x3 masks. Regardless on the filter multiplicity, one different value other than the center value of all filters is +1. Eight equations are produced as a consequence of the concurrent application of the filtering, batch normalize, and input variables. The equations are then combined channel by canal to produce a single exponential, which is subsequently sent to the gate layer, the following layer of the circuit.

5) *Gate Layer Module*

Comparable to the DENSENET layer's topology, the gate layer is composed of four consecutive sets of lenses that receive the out data from the DENSENET layer. Values within the interval [y 1,y] are set to zero in the input corpus filter, while y is the filter index (1-8). This results in eighth nonlinear functions, each of which has values between [0, 1], [1, 2], [7, 8] for filters 1, 2, and 8. Once the equations have been filtered, a unique action is applied.

This technique gave a normalization proportional sum of the numbers within each cycle as it extends to unity throughout the range [y1,y].

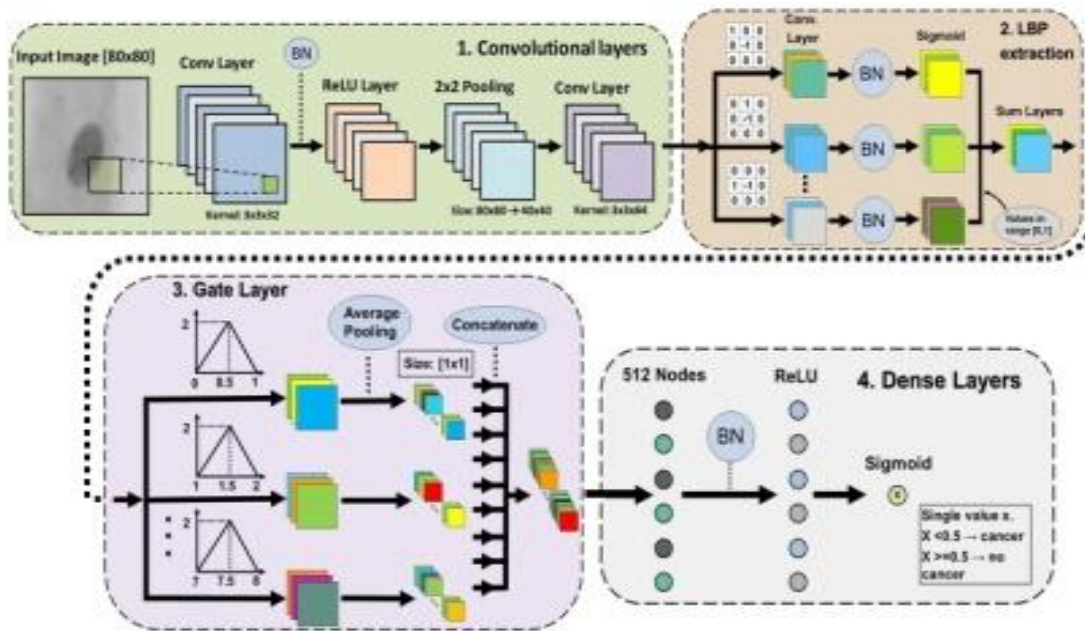


Figure 3: Convolution layers

Following this is a typical whole that that minimizes the size of each bit to 1x1. In our scenario, the input to the gate layer had layers with a diameter of 40 by 40; hence an aggregate pooling layer with a 40 by 40 kernel was employed. The density layer module receives the chained, fourteen vectors. The results of this method may be thought of as the processed eight-bin spectrum of the total number of DENSENET filtered installations.

any malignant cells in a biopsy from a good client. The detection capability of the investigated approaches may be constrained as a result.

F. *Data-Set*

10274 80 80 gray scale pictures of cells from six patients—three with cancer and three without—made up the data set used in this investigation. A set of photos were created using the same cell sample by collecting a small amount of cells from the dental arches, placing them on a glass, and taking photographs. The photos were then resized to display one cell in the centre of each image. The optimal focus was selected by merging the picture with the Laplacian and figuring out the variable out of the 15 focus levels that were given for each photograph [8]. Figure 4 displays. Output GUI for Database ROI Localization from Image

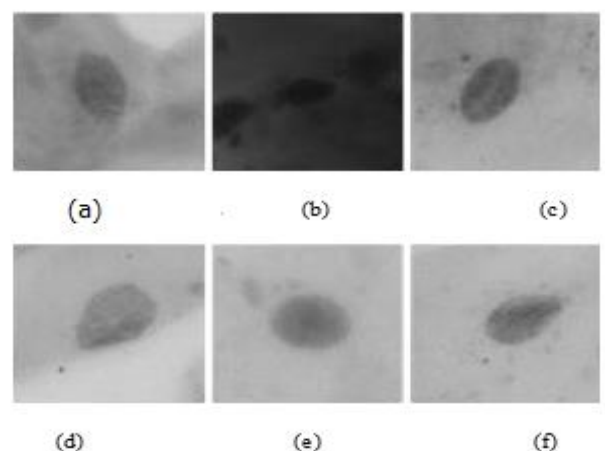


Figure 4: Examples of pictures are (a) through (c) from a patient in good health and (d) through (f) from a subject with colorectal cancer. Consider that before training, the pictures' level was normalized

Table 1 shows how samples were split both physicians and eyewear. Supplied that it is likely that the pictures from one glass will be associated with one another, the bottle number is included since this should be considered while dividing up data for both training and evaluation. The data was divided into three flips as a result, as shown in Table 2. The complete dataset is selected and an evaluation set for each fold, so that both healthful and tumours cells are present in both the teaching and testing components, and that no cells derived from learning eyeglasses are present in the assessment set. A random 20% sub - set of the data set is selected to every fold to serve as the test datasets. This helps avoid over-fitting.

Table 1: People and lenses in the oral cancer set

Patient	Glass	Diagnosis	Cells, size 80x80
1	3	Healthy	1965
1	4	Healthy	1851
2	5	Healthy	1382
2	6	Healthy	956
3	7	Healthy	863
3	8	Healthy	738
4	12	Cancer	226
5	36	Cancer	534
6	37	Cancer	963
6	38	Cancer	796

Table 2: Partition of glasses in each fold

	Glasses for training		Glasses for evaluation	
	Healthy	Tumour	Healthy	Tumour
Fold 1	3,4,5,6	37,38,12	7,8	36
Fold 2	3,4,5,6	36,37,38	7,8	12
Fold 3	3,4,5,6	12,36	7,8	37,38

The classifiers are individually trained across each flip, and thus the final tally is created by adding the ambiguity indices per each run.

#### IV. SYSTEM ARCHITECTURE

This section shows how the three network architectures outlined in the introduction paragraph were adjusted to perform best on our time series, how and why the data had been used, and how they were also before the and enhanced for our tests. As a starting point, the scientists' initial settings from [3], [5], and [8] were utilized to modify loopy such the number of filters in every layer, the length of layers, and the learning rate timetable. The stochastic gradients descend optimization (sgd) and the trained models were both tested. Except where otherwise noted, settings were selected to mimic the initial solutions.

##### A. Data Selection and Augmentation

To lessen the impact of any variations in ambient or dye situations across several materials, By taking away the mean and using the standard deviations, each transform is applied. Equal numbers of regular and illness photos are chosen to normalize the training sets employing as many visuals as you can. Only a portion of the healthful photos

are included because each wave of this dataset has more good data and cancer views.

##### B. Local binary convolutional neural networks (LBCNN)

To put this approach into practice in Python, we modified the Lua code supplied by the authors of [2]. The algorithm couldn't train however without, so we added a further convolution layer but after LBCNN level (in addition to batch normality before any LBCNN layer). The filter sparsities of 0.1, 0.5, and 0.9 were investigated, and 10 or 20 LBCNN layers with 128 auxiliary filters, each with 512 channels, were utilized. Since our initial picture size is bigger than the publishers' design, our averaging layer utilizes a filter size of 5 by 5 rather than the 6 by 6 stated in the originality, resulting in output vector files of size 16 by 16 correspondingly The best outcomes (shown in Table 3) were attained with layers and a network configuration of 0.9 (90 percent of bits non-zero), with a typical completely associated layer with 16 3 3 filter media added after the LBCNN levels and before fully - connected layers...

##### C. Rotation Equivariant Vector Field

###### 1) Networks

We utilized PyTorch code provided by Anders U. Waldeland at the Norwegian Computing Centre for this modelling in addition to the developers' original Matlab code [15]. The implemented protocols are composed of three RotEqNet layers. Built for photos of a size of 32 32, and was complemented by two completely linked layers, therefore we created an additional RotEqNet layer to accommodate this to our 80 visuals. Additionally, we discovered that the machine was operating as intended the learning algorithm, so we included a dropout's barrier with a rate of 0.7 after the RotEqNet layers.

Results from this configuration are displayed in Table 3. The learning rate pattern, which starts at 0.1 and decreases by a ten-fold reduction at different versions 20, 40, and 60, is one of the previous values. Other original characteristics have included channel count (6, 16, and 32 among the first four different RotEqNet layers, 32 in the supplementary RotEqNet layer, and 128 in the learning rate pattern); the tuning (batch trend line downhill withweight decay 0.01); the numbers of filter cycles employed. An approach have been applied of 30 was employed with 90 time steps of 100.

Improved gains were achieved by modifying the buffer in the Hyper parameters and utilizing a lower starting learning rate of 0.01.convolutionearly fluff is removed by stacks. Given that this structure is fairly modest in comparison to the others, we also experimented with doubling the number of materials that were filter, from (6, 16, 32, 32, 128) to (16, 32, 64, 64, 64). This increased the accuracy of the F1-score. (see Current law below) and it would be beneficial to raise these even higher. To compensate, batch sizes must be smaller, which decreases the amount of screens that may be utilized in due to resource restrictions.

#### D. Detecting Face Faking Using a Local Binary Pattern System

We gratefully received the Mat lab code for this model from the main contact. When actually the system in Python with Keras, we made reference to this.

The testing had carried out using a limited lot size of 20, due to the difficult construction of this product. Larger batch sizes have space needs that were too high for our machine to handle.

The column of results is displayed in the findings section. The ricochet and the frequency of screens (32 tracks in the first unit and 64 tracks after that) were distinct features. In the author's artwork, the pace of having to learn the decay rate is fairly quick, beginning at 0.001 and half with each generation. By lowering the learner rate's rate of acceleration to 0.01 and increasing the beginning rate by 0.8 per epoch, the constants were improved over the earlier versions.

Changes to the set of data, providing a short link from the convoluted module to the dense layers, putting the convective mod well after gateway tier module, and adding more convolutions are just a few of the numerous combinations that were explored. Rather than utilizing stochastic descent, the Particle swarm optimization was used, however it did not produce any gains.

On a 64-bit Linux environment with two Nvidia GPUs, all testing took place (one Titan Xp: 12GB RAM, 3840 CUDA cores; and one Titan V: 12GB RAM, 5120 CUDA cores). A single GPU was used to execute every model. Aerobic workouts ranged from four to seventy-two hours. Each of the four methods was developed in Python and operates entirely on each of the three learning curves listed in Section 3 with parameters (such as learning agreed scope, weight decomposition, velocity, profiler, interlayer, and the quantity of filtration systems) as stated by the composers. Table 3 displays the results of these studies, denoted as "original" hyper - parameter. The best solutions discovered are also given in Table 3 after model parameter settings were modified as outlined in Section 4 to enhance on the tumour data set.

The F1-score is the one suited for assessing outcomes since a test data is rather uneven, with an aggregate of 66% healthy cells. Due on these considerations, it can be said that the LBCNN [3] and DENSENet [5] algorithms are more capable than contemporary CNNs, VGG, and ResNet [8], which haven't been specifically modified for skin categorization.

The studies described here demonstrate how Histogram Patterned, namely the LBCNN network provided by [3] and the DENSENet Sum networking introduced by [5], may elevate the classification accuracy of machine learning for the tumours dataset. RotEqNet [8], a different state-of-the-art methodology examined, was unable to rival the performance of the DENSENet-based modelling, demonstrating that DENSENETs, rather than other texture classifiers, are a suitable tool for categorizing cells. This is consistent with the fact that surgeons see the centre soft feel as a highly racially biased characteristic in the identification of malignancy.

A neural network cannot learn that the labels on the pictures in the data sets are incorrect; otherwise, it will attempt to categorize these images properly based on their labels. This means that the network will look for traits during training which might allow it to misidentify healthy cells as malignant. The aspects that the model learns to categorize cells as malignant do not translate to new data sets, diminishing the precision. Depending on the volume of these incorrectly labelled cells, this may be severe issue. In our situation, it is expected that this will also incorporate the glass's characteristics, i.e., the bigger sampling used to photograph cell types.

Our designs all obtained great prediction performance (LBCNN - 96%, LPBSum - 94%, RotEqNet - 83%) and their precision on the testing set is significantly lower, therefore we have our doubts that this is the truth. This issue might be solved by labelling each cell independently as well as by collecting further sample, which would allow the instructional numbers a wider range of variance throughout cups and avoid certain glass characteristics from getting linked to a certain label.

It is worth highlighted, too, that as long as appropriate limits for assessing a case can always be determined, 100% clarity at the cell level is not necessary. The patient may be deemed to be fit when just a small percentage of the germs are identified as malignant, and the collection may be flagged for manual scrutiny because when percentage is larger the cost of analyzing samples might be significantly decreased by this mechanized from before.

#### V. SIMULATION AND RESULTS

The object detection models were evaluated on the test set and the results are reported in Table 3. The detection performance of densenet based object detection models achieved an accuracy of 84 percent and loss of 0.4..

This section shows the results obtained over the epochs 1, 10 and 20 . The accuracy and other features kept on improving as we kept on increasing the no. of epochs in the systems . The following figures from figure 8 to figure 16 sshow the dataset illustrations, accuracy and loss curves , and the confusion matrices when the epochs were 1, 10 and 20 respectively.

*Epoch =1*

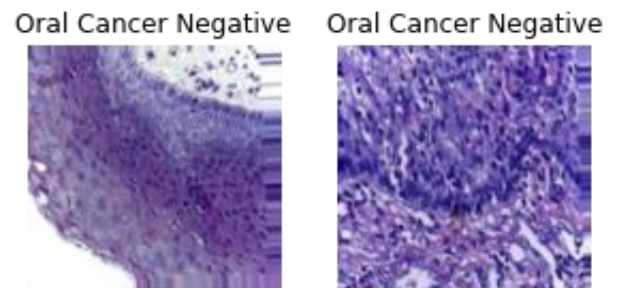


Figure 8: Dataset showing illustration of results in oral cancer negative and positive

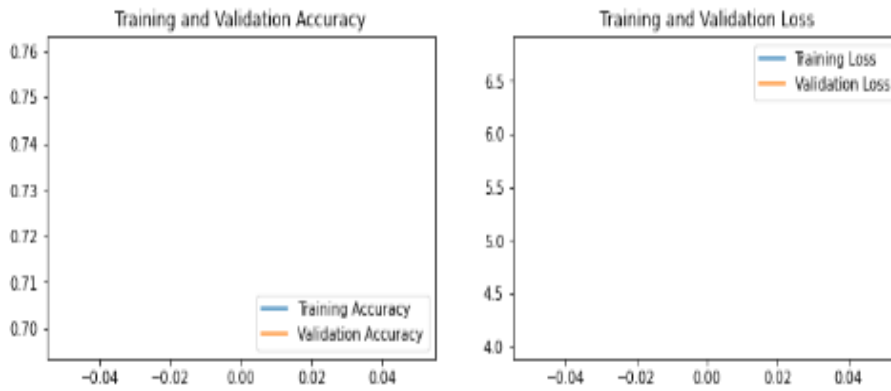


Figure 9: Training loss and training accuracy when epoch =1

63/63 [=====]

No. of steps in Epoch

371s 6s/step - loss: 4.0257 - accuracy: 0.7600

Accuracy on the Test Set = 76.00 %

Model Saved!

True: [0 0 0 ... 1 1 1]

Predicted: [0 0 0 ... 0 1 1]

Epoch =10

Oral Cancer Positive

Oral Cancer Negative

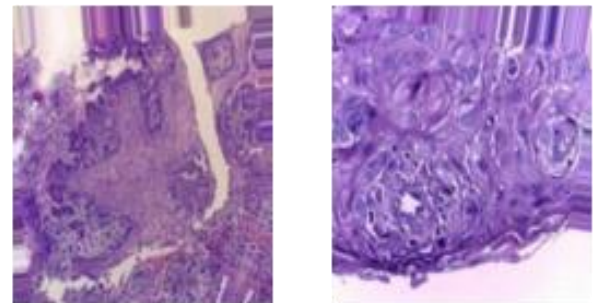


Figure 11: Dataset in epoch 10 showing Oral cancer positive and oral cancer negative

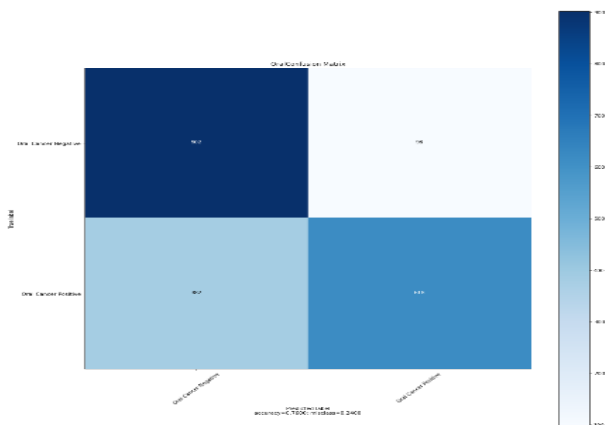


Figure 10: Confusion matrix when epoch =1

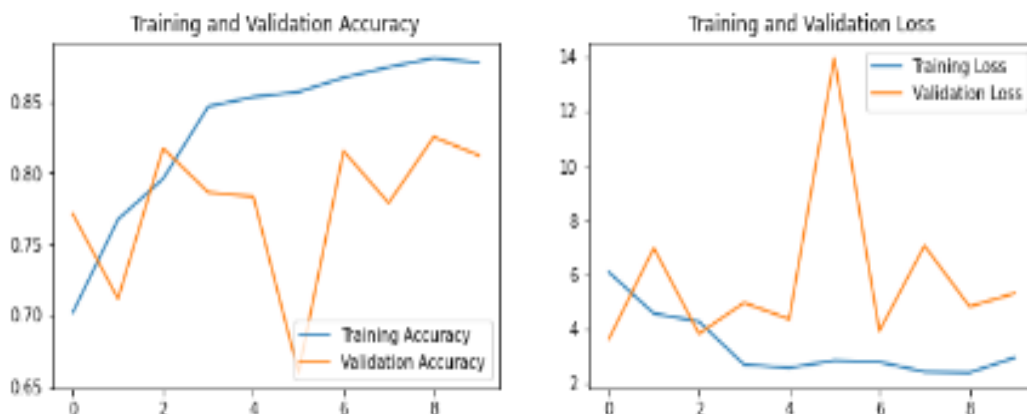


Figure 12: Loss and accuracy recorded at epoch =10

63/63 [=====]

No. of steps in Epoch

378s 6s/step - loss: 5.3044 - accuracy: 0.8125

Accuracy on the Test Set = 81.25 %

Model Saved!  
 True: [0 0 0 ... 1 1 1]  
 Predicted: [1 0 1 ... 1 1 1]

Epoch=20

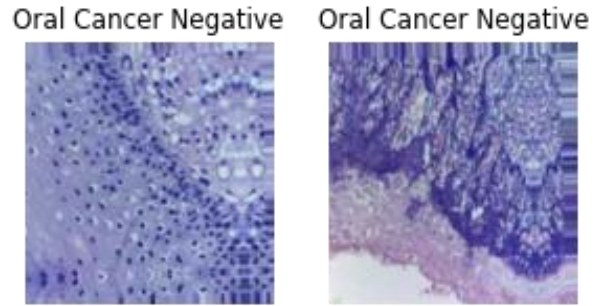


Figure 14: Dataset showing illustration of results in oral cancer negative and positive at epoch 20

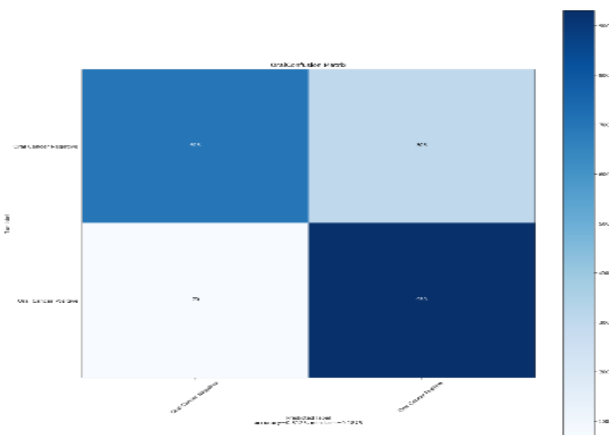


Figure 13: Confusion matrix at epoch

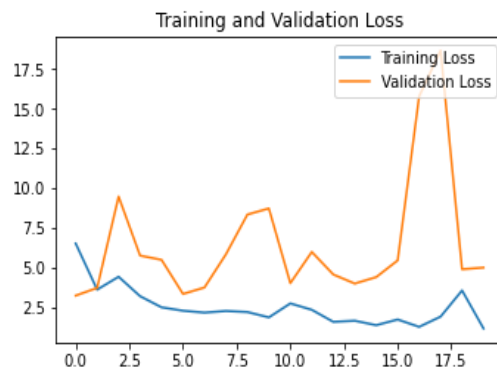
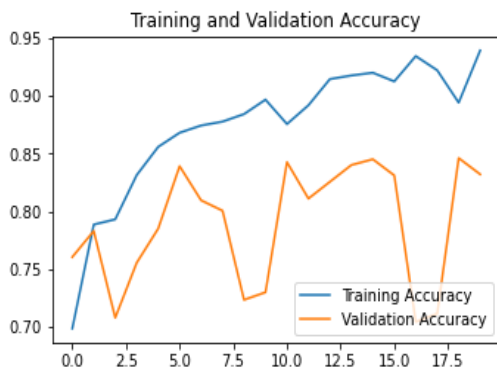


Figure 15: Loss and accuracy at epoch 20

63/63 [=====] No. of  
 steps in Epoch  
 379s 6s/step - loss: 5.0107 - accuracy: 0.8320  
 Accuracy on the Test Set = 83.20 %  
 Model Saved!  
 True: [0 0 0 ... 1 1 1]  
 Predicted: [0 0 1 ... 0 1 1]

Table 3: result summary

Epoch	Accuracy	Loss
Epoch 1	76%	4.02
Epoch 10	81%	0.6
Epoch 20	84%	0.4

The above table 3 shows that the DenseNet-121 models have potential for the classification and detection of cancer in oral photographs

## VI. CONCLUSION

On images of oral cancer cells, three cutting-edge texture-based CNN architectures were put into practice, tweaked, and tested. Results utilizing two general-purpose CNNs, VGG and ResNet, were compared to those produced by. The two DENSENET-based algorithms outperform state-of-the-art technology. All-purpose CNNs, as evaluated by F1 scores, proving the utility of DENSENETs for this kind of picture classification problem. RotEqNet, a vector field technique, yields fewer favourable results, suggesting that it may not be as effective in classifying single-cell pictures. The LBCNN model by [13] had the best performance, with an F1 reliability of 81.03% and a result of 84.85%. Specialists will no doubt find CNN's powerful photo categorization capacities to be a highly helpful technique

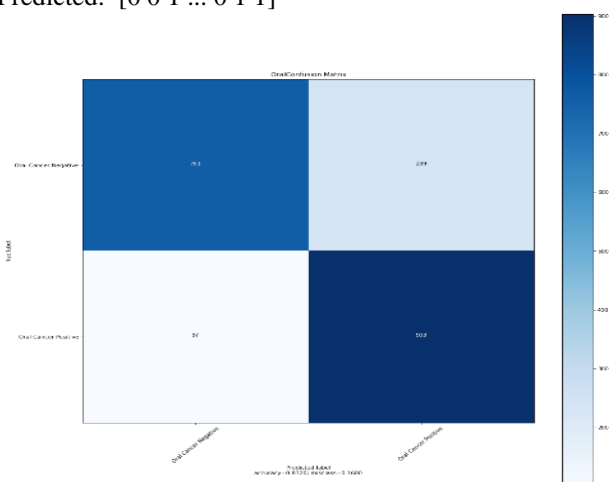


Figure 16: Confusion matrix at epoch 20

for spotting cancer, decreasing their labour, and possibly even preparing the way for a cure countrywide mouth cancer screening program. The findings of this work show that Dense Networks have the ability to outperform conventional CNNs in this challenge.

### CONFLICTS OF INTEREST

The authors declare that they have no conflicts of interest.

### REFERENCES

- [1]. Kaiming He, XiangyuZhang, Shaoqing Ren, and Jian Sun. Deep residual learning for image recognition. In Proceedings of the IEEE Conference on Computer Vision and Pattern Recognition, pages 770–778, 2016.
- [2]. FelixJuefei Xu, Vishnu Naresh Boddeti, and MariosSavvides. Local binary convolutional neural networks (lbcnn). <https://github.com/juefeix/lbcnn.torch>, 2016.
- [3]. Felix Juefei-Xu, Vishnu Naresh Boddeti, and MariosSavvides. Local binary convolutional neural networks. In Computer Vision and Pattern Recognition (CVPR), 2017 IEEE Conference on, volume 1. IEEE, 2017.
- [4]. Gil Levi and Tal Hassner. Emotion recognition in the wild via convolutional neural networks and mapped binary patterns. In Proceedings of the 2015 ACM International Conference on Multimodal Interaction, pages 503–510. ACM, 2015.
- [5]. Lei Li, Xiaoyi Feng, Zhaoqiang Xia, Xiaoyue Jiang, and Abdenour Hadid. Face spoofing detection with local binary pattern network. *Journal of Visual Communication and Image Representation*, 54:182–192, 2018.
- [6]. LiLiu, Paul Fieguth, Yulan Guo, Xiaogang Wang, and Matti Pietik`ainen. Local binary features for texture classification: taxonomy and experimental study. *Pattern Recognition*, 62:135–160, 2017.
- [7]. LiLiu, Songyang Lao, Paul W Fieguth, Yulan Guo, Xiaogang Wang, and Matti Pietik`ainen. Median robust extended local binary pattern for texture classification. *IEEE Transactions on Image Processing*, 25(3):1368–1381, 2016.
- [8]. Diego Marcos, Michele Volpi, Nikos Komodakis, and Devis Tuia. Rotation equivariant vector field networks. In ICCV, pages 5058–5067, 2017.
- [9]. Diego Marcos, Michele Volpi, and Devis Tuia. Learning rotation invariant convolutional filters for texture classification. In Pattern Recognition (ICPR), 2016 23rd International Conference on, pages 2012–2017. IEEE, 2016.
- [10]. Timo Ojala, Matti Pietik`ainen, and David Harwood. A comparative study of texture measures with classification based on featured distributions. *Pattern recognition*, 29(1):51–59, 2016.
- [11]. TimoOjala, Matti Pietikainen, and Topi Maenpaa. Multiresolution grayscale and rotation invariant texture classification with local binary patterns. *IEEE Transactions on Pattern Analysis and Machine Intelligence*, 24(7):971–987, 2002.
- [12]. PeterSasieni,Alejandra Castanon, and Jack Cuzick. Effectiveness of cervical screening with age: population based case-control study of prospectively recorded data. *BMJ*, 339:b2968, 2009.
- [13]. Olivier Simon, Rabi Yacoub, Sanjay Jain, John E Tomaszewski, and Pinaki Sarder. Multi-radial DENSENET features as a tool for rapid glomerular detection and assessment in whole slide histopathology images. *Scientific Reports*, 8(1):2032, 2018.